Nano Research

Open Access

Research Article

High-performance flexible thermoelectric generators with planar and multilayer-stacked structures for wearable electronics

Jing Guo[1], Jiahao Zhou[2], Bingzheng Zhang[3], Wei Yu[3], Mingcen Weng[4,5] ✉, Qiaohang Guo[3] ✉, Zhiqing Li[5,6], and Hechen Ren[1,6,7] ✉

[1] *The International Joint Institute of Tianjin University, Fuzhou, Tianjin University, Tianjin 300072, China*
[2] *College of Chemical Engineering, Fuzhou University, Fuzhou 350108, China*
[3] *School of Materials Science and Engineering, Fujian University of Technology, Fuzhou 350118, China*
[4] *Institute of Biology and Chemistry, Fujian University of Technology, Fuzhou 350118, China*
[5] *Department of Physics, Tianjin University, Tianjin 300350, China*
[6] *Tianjin Key Laboratory of Low Dimensional Materials Physics and Preparing Technology, School of Science, Tianjin University, Tianjin 300072, China*
[7] *Center for Joint Quantum Studies, Department of Physics, School of Science, Tianjin University, Tianjin 300350, China*

Cite this article: *Nano Research*, **2026**, *19*, 94908713. https://doi.org/10.26599/NR.2026.94908713

ABSTRACT: Flexible thermoelectric generators (f-TEGs) can directly convert low-grade thermal energy from the human body and surrounding environment into electricity, showing great promise for wearable power systems and self-sustained sensors. However, conventional inorganic thermoelectric materials still face significant constraints in balancing flexibility, structural stability, and energy conversion efficiency. In this work, high-performance Bi_2Te_3/hydroxypropyl methylcellulose (HPMC)@paper composite thermoelectric films were fabricated via a vacuum filtration method, realizing a synergistic enhancement in both flexibility and thermoelectric performance. The obtained p-type and n-type films exhibited Seebeck coefficients of 182.96 and −229.98 μV·K^{-1}, respectively, and maintained stable output under repeated bending. Based on these films, both planar and multilayer stacked f-TEG architectures were designed to achieve multidimensional energy harvesting. The Level-III stacked f-TEG reached an ultrahigh device-level Seebeck coefficient (S_{device}) of 11,330.25 μV·K^{-1} and a maximum output power of 617.4 nW, demonstrating outstanding conversion capability and structural robustness. When integrated with an Ecoflex substrate, the device maintained stable operation under bending, twisting, and conformal attachment to curved surfaces. A smart wristband built from this system continuously drove a low-power pedometer during human-wear testing, validating its feasibility for wearable thermoelectric energy harvesting. This study proposes an inorganic–organic hybrid thermoelectric film design that combines high flexibility with excellent thermoelectric performance, offering a new strategy for flexible energy devices and showing broad prospects in wearable electronics.

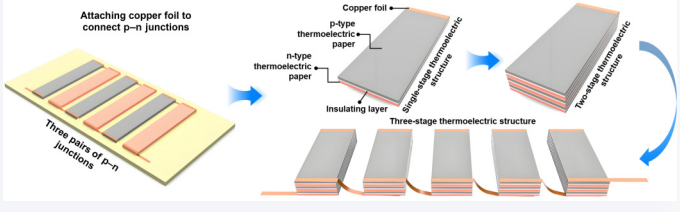

KEYWORDS: flexible thermoelectric generator, Bi_2Te_3/hydroxypropyl methylcellulose (HPMC)@paper, wearable electronics, stacked architecture

1 Introduction

Thermoelectric (TE) technology enables the direct conversion of heat into electricity, offering a promising route toward sustainable energy harvesting and thermal management in the era of distributed electronics [1–6]. Owing to their compactness, reliability, and solid-state operation, TE materials have been widely applied in aerospace, medical, and wearable devices [7–12]. Compared with conductive polymers or carbon-based materials, inorganic thermoelectric materials generally exhibit higher power factors (PFs) and better long-term stability, making them more suitable for high-efficiency device fabrication and application. However, the rigid and brittle nature of conventional inorganic thermoelectric materials limits their integration with flexible or curved surfaces, which are essential for next-generation wearable systems. Among various TE materials, Bi_2Te_3 and its derivatives remain the most efficient near-room-temperature systems due to

Received: November 19, 2025; **Revised:** March 12, 2026
Accepted: April 6, 2026

✉Address correspondence to Mingcen Weng, wengmc@fjut.edu.cn; Qiaohang Guo, guoqh@fjut.edu.cn; Hechen Ren, ren@tju.edu.cn

their high electrical conductivity (σ) and low thermal conductivity [13]. Over the past decade, extensive efforts have focused on improving their mechanical compliance and processability through structural engineering and polymer hybridization. For example, Li et al. [14] fabricated polyvinylidene fluoride (PVDF)-hexafluoropropylene (HFP)/Bi_2Te_3 core–shell nanofiber films that achieved synergistically enhanced piezoelectric and thermoelectric effects, along with excellent mechanical flexibility (elastic modulus = 8.87 MPa) and high breathability (1235 $g{\cdot}m^{-2}{\cdot}day^{-1}$). Guo et al. [15] prepared Bi_2Te_3/silk-fibroin composite films via evaporation-assisted self-assembly, achieving Seebeck coefficients (S) of 199 $\mu V{\cdot}K^{-1}$ (p-type) and −240 $\mu V{\cdot}K^{-1}$ (n-type). Mao et al. [16] developed a scalable physical vapor deposition (PVD) method combined with homogeneous-layer fusion to produce flexible n-type Bi_2Te_3 films with an exceptional power factor of 30.0 $\mu W{\cdot}cm^{-1}{\cdot}K^{-2}$. Despite these advances, flexible inorganic thermoelectrics still suffer from a trade-off between thermoelectric performance and mechanical compliance, limiting their practical use in wearable energy-harvesting devices. Meanwhile, thermoelectric gels have emerged as an important class of organic materials for wearable electronics [17, 18]. For example, Li et al. [19] reported a self-powered multimodal fingertip receptor based on thermogalvanic hydrogels, in which thermovoltage signals enabled rapid material recognition within 80 ms. This highlights the promise of gel-based systems in self-powered sensing and human–machine interfaces. However, because such systems mainly rely on ionic or thermogalvanic processes, Bi_2Te_3-based electronic thermoelectric materials remain more attractive for wearable power modules requiring continuous output, high conductivity, and structural stability.

Flexible thermoelectric generators (f-TEGs) have recently emerged as an appealing solution for harvesting low-grade heat from the human body and ambient environment to drive self-sustained electronics and wearable sensors [20, 21]. However, the practical development of f-TEGs still faces several challenges. Most flexible systems suffer from inefficient heat collection and low energy conversion efficiency, primarily due to their planar geometry that restricts the effective contact area with non-flat or dynamic heat sources. Furthermore, achieving stable electrical output under repeated mechanical deformation remains difficult because of weak interfacial adhesion and mechanical–electrical decoupling between the thermoelectric layers and polymer substrates [22–26]. Recent studies have demonstrated that rationally designed multilayer, serpentine, and origami-inspired architectures can substantially improve the thermal–mechanical coupling efficiency of flexible thermoelectric materials [27–29]. However, these complex designs often involve cumbersome fabrication processes or poor scalability, limiting their widespread adoption. Consequently, it remains crucial to develop a simple yet effective material–structure-integrated strategy capable of achieving high thermoelectric output, robust mechanical durability, and scalable manufacturability within a unified framework.

To address these challenges, we propose a flexible inorganic–organic hybrid composite based on Bi_2Te_3 and hydroxypropyl methylcellulose (HPMC), in which nanoscale Bi_2Te_3 platelets are embedded within an elastic HPMC network. The hybrid films, fabricated via vacuum filtration, simultaneously exhibit high Seebeck coefficients (182.96 $\mu V{\cdot}K^{-1}$ for p-type and −229.98 $\mu V{\cdot}K^{-1}$ for n-type) and excellent bendability. Compared with our previously reported Bi_2Te_3/silk fibroin (SF) composite films, the Bi_2Te_3/HPMC@paper in this work retains comparable thermopower while exhibiting markedly enhanced electrical conductivity and power factor, thereby enabling improved device-level output performance. Building on this material platform, both planar and multilayer stacked f-TEG configurations were designed to realize multidimensional energy harvesting. The Level-III stacked f-TEG achieves an ultrahigh device-level Seebeck coefficient (S_{device}) of 11,330.25 $\mu V{\cdot}K^{-1}$ and a maximum output power ($P_{out,max}$) of 617.4 nW, maintaining stable performance under mechanical deformation. Furthermore, the integrated device can conformally attach to human skin to harvest body-surface waste heat, thereby enabling a smart wristband demonstration with continuous pedometer operation. This work establishes a universal strategy for coupling inorganic thermoelectric domains with flexible polymer matrices and structural hierarchy, providing a practical pathway toward high-output, mechanically durable, and wearable thermoelectric energy systems.

2 Results and discussion

2.1 Fabrication and characterization of Bi_2Te_3/HPMC @paper

The fabrication process of the Bi_2Te_3/HPMC@paper is illustrated in Fig. 1(a). Flexible Bi_2Te_3/HPMC@paper was prepared by vacuum filtration. The interfacial morphology and structural characteristics of the obtained films were systematically characterized. The surface scanning electron microscopy (SEM) images of the p-type and n-type Bi_2Te_3/HPMC@paper (Figs. 1(b) and 1(f)) reveal that both samples consist of well-defined plate-like Bi_2Te_3 microcrystals forming a compact, layered network structure [15]. Cross-sectional SEM images (Figs. 1(c) and 1(g)) reveal a distinct stratified morphology, in which Bi_2Te_3 particles are predominantly concentrated in the lower layer, whereas the upper layer is enriched with HPMC. This vertical compositional difference effectively enhances interfacial adhesion and stabilizes thermoelectric transport. Cross-sectional energy dispersive X-ray spectroscopy (EDS) elemental mappings of the p-type Bi_2Te_3/HPMC@paper are shown in Figs. 1(d) and 1(e). The Sb $L\alpha_1$ and Te $L\alpha_1$ maps indicate that Sb and Te are predominantly concentrated in the bottom region of the specimen (in the current cross-sectional orientation), confirming their association with the thermoelectric powders and further supporting the well-defined layered architecture of the composite. For the n-type Bi_2Te_3/HPMC@paper, the Bi $M\alpha_1$ and Te $L\alpha_1$ elemental maps (Figs. 1(h) and 1(i)) likewise show Te enrichment in the bottom region, consistent with the stratified morphology observed for the p-type counterpart. Collectively, these EDS mappings demonstrate continuous elemental distribution across the Bi_2Te_3/HPMC@paper interface, corroborating the good dispersion of the thermoelectric powders within the composite and the formation of a distinct layered structure. The flexible HPMC layer not only serves as a mechanical support phase, imparting excellent durability, but also helps alleviate stress concentration among Bi_2Te_3 particles during deformation. X-ray diffraction (XRD) results (Fig. 1(j)) show that the pure filter paper exhibits only a broad amorphous cellulose peak, whereas the Bi_2Te_3/HPMC@paper displays sharp diffraction peaks at 2θ = 27.6°, 37.9°, and 42.3°, corresponding to the characteristic peaks of Bi_2Te_3 in the standard JCPDS card [30]. The sharp peak shapes and absence of impurity peaks confirm that the Bi_2Te_3 crystal structure

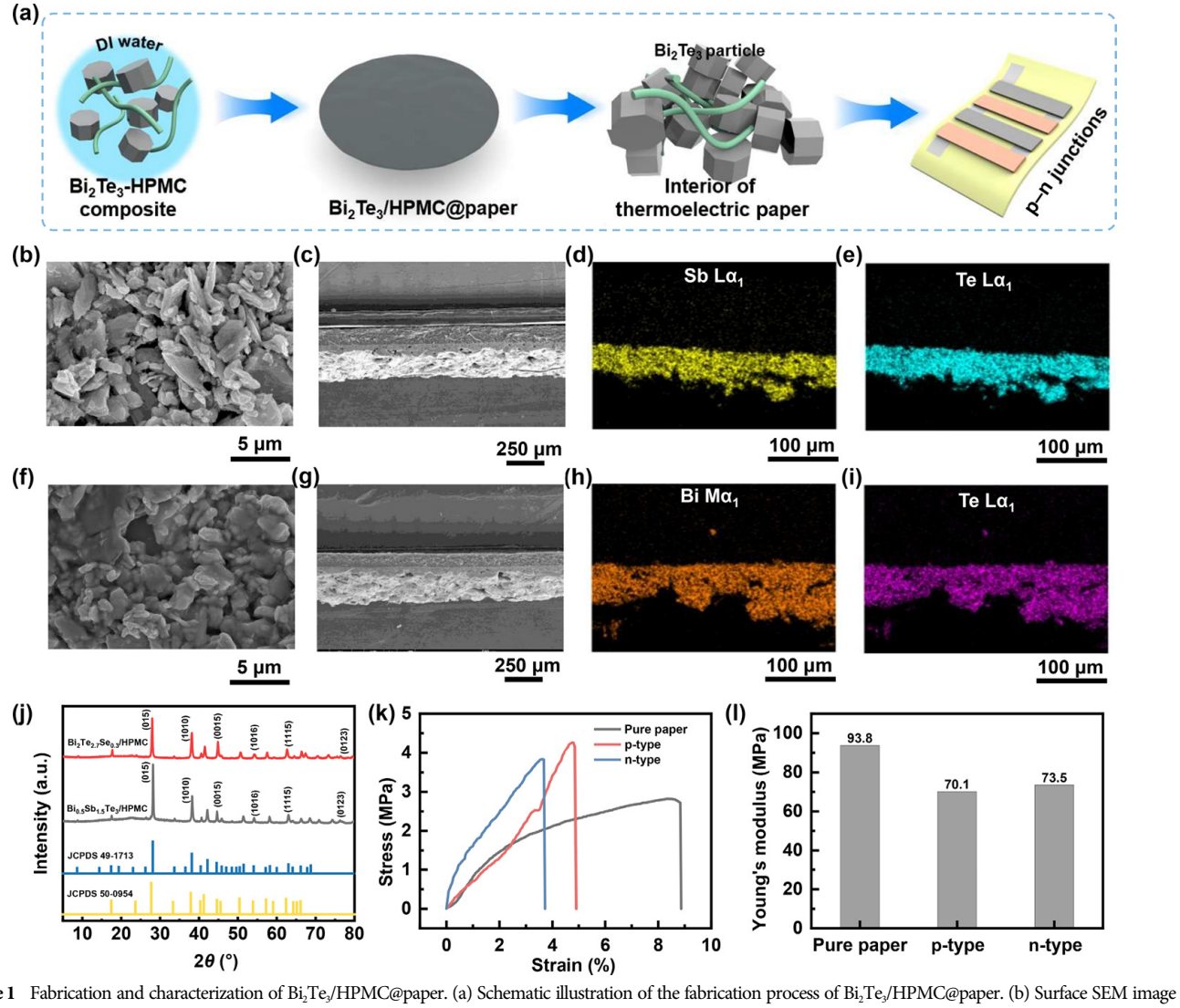

Figure 1 Fabrication and characterization of Bi_2Te_3/HPMC@paper. (a) Schematic illustration of the fabrication process of Bi_2Te_3/HPMC@paper. (b) Surface SEM image of the p-type Bi_2Te_3/HPMC@paper. (c) Cross-sectional SEM image of the p-type Bi_2Te_3/HPMC@paper. (d) Cross-sectional Sb $L\alpha_1$ elemental mapping of the p-type Bi_2Te_3/HPMC@paper. (e) Cross-sectional Te $L\alpha_1$ elemental mapping of the p-type Bi_2Te_3/HPMC@paper. (f) Surface SEM image of the n-type Bi_2Te_3/HPMC@paper. (g) Cross-sectional SEM image of the n-type Bi_2Te_3/HPMC@paper. (h) Cross-sectional Bi $M\alpha_1$ elemental mapping of the n-type Bi_2Te_3/HPMC@paper. (i) Cross-sectional Te $L\alpha_1$ elemental mapping of the n-type Bi_2Te_3/HPMC@paper. (j) XRD patterns of the p-type and n-type Bi_2Te_3/HPMC@paper. (k) Stress–strain curves of Bi_2Te_3/HPMC@paper. (l) Young's modulus of Bi_2Te_3/HPMC@paper.

remains intact and highly crystalline. Fourier transform infrared (FTIR) spectra (Fig. S1 in the Electronic Supplementary Material (ESM)) further reveal weak interactions between Bi_2Te_3 and HPMC. Both p-type and n-type composites exhibit characteristic absorption bands of HPMC within 4000–500 cm^{-1} (–CH_2/–CH_3 stretching at 2914 cm^{-1} and –OH vibration near 639 cm^{-1}), with slight peak shifts and intensity variations, indicating the presence of hydrogen bonding or electrostatic interactions between the inorganic and organic phases [31]. As shown in the Raman spectra (Fig. S2 in the ESM), both p-type $Bi_{0.5}Sb_{1.5}Te_3$ and n-type $Bi_2Te_{2.7}Se_{0.3}$ exhibit characteristic low-wavenumber lattice-phonon modes typical of the Bi_2Te_3 family, whereas HPMC and the paper substrate mainly contribute broad background features [32]. In the composites, these phonon signatures remain discernible but show attenuated intensity accompanied by subtle lineshape changes, indicating that HPMC coating does not disrupt the crystalline structure of the inorganic phase while suggesting interfacial molecular-level confinement and charge redistribution. This behavior is consistent with the proposed hydrogen-bonding and electrostatic adsorption interactions between the hydroxyl/ether functionalities of HPMC and the Bi_2Te_3-based surface. Compared with previously reported defect-engineered Bi_2Te_3 single crystals [33], the Bi_2Te_3/HPMC@paper developed in this work exhibits excellent bendability and practical mechanical compliance. The tensile stress–strain curves (Fig. 1(k)) of pure filter paper and the p-type and n-type Bi_2Te_3/HPMC@paper demonstrate that the pure filter paper substrate has a tensile strength of approximately 2.8 MPa and a fracture strain of 6%–7%, indicating limited ductility. After composite formation, the tensile strengths increase to 4.2 MPa (p-type) and 4.5 MPa (n-type), suggesting enhanced load-bearing capacity due to the incorporation of Bi_2Te_3 particles. Meanwhile, as shown in Fig. 1(l), the Young's modulus decreases slightly from 93.8 MPa to approximately 70.1 MPa (p-type) and 73.5 MPa (n-type), implying improved elasticity and toughness. As shown in Table S1 in the ESM, compared with previously reported Bi_2Te_3-based thermoelectric films, the Bi_2Te_3/HPMC@paper developed in this work exhibit

more competitive overall performance in terms of key thermoelectric metrics, which further highlights the advantages of employing HPMC as the organic polymer matrix in constructing the composite film [15, 34–37]. In summary, the introduction of the flexible HPMC support phase effectively enhances the mechanical stability and deformation adaptability of the Bi_2Te_3/HPMC@paper, providing a robust structural and performance foundation for the subsequent fabrication of flexible thermoelectric devices.

2.2 Thermoelectric properties of Bi_2Te_3/HPMC@paper

In this study, the TE effect of the Bi_2Te_3/HPMC@paper primarily originates from carrier (electron and hole) migration driven by a temperature difference (ΔT), namely the Seebeck effect [38–40]. When a ΔT is established across the material, charge carriers at the hot side gain higher energy and diffuse toward the cold side, generating an internal potential difference. As the diffusion current and the resultant drift current counterbalance each other, a steady thermoelectric voltage is formed between the two ends of the film. In p-type Bi_2Te_3/HPMC@paper, holes are the dominant charge carriers, and the voltage direction points from the hot side to the cold side. In contrast, for n-type films, electrons dominate the transport process, and the voltage direction is reversed [15]. The output signals acquired from the TE film are captured by using a homemade measurement system (Fig. S3 in the ESM). To ensure the accuracy of the results, the Seebeck coefficient and electrical conductivity were measured using high-precision commercial instruments. The hot-end temperature of the Bi_2Te_3/HPMC@paper was controlled by a thermostatically adjustable heating platform (JF-956S) with an accuracy of ±1 °C. The temperature difference between the two ends of the film was measured using a contact thermocouple thermometer (UNI-T, UT325) with an accuracy of ±1 °C. The electrical signals between the hot and cold ends were recorded with a benchtop digital multimeter (UNI-T, UT805A+), with an accuracy of ±(0.015% of reading + 3 digits). During the measurements, highly conductive silver adhesive and copper electrodes were employed to minimize the influence of contact resistance between the sample and the instruments on the measured outputs. The thermoelectric parameters of the p-type and n-type Bi_2Te_3/HPMC@paper are summarized in Fig. S4 in the ESM, including the S, σ, and PF. The p-type Bi_2Te_3/HPMC@paper exhibits a positive S, as the Bi_2Te_3-to-HPMC mass ratio increases from 6:1 to 14:1, the S value first increases and then decreases, with BTHP-10 (BTHP-10 refers to the Bi_2Te_3/HPMC@paper sample prepared with a Bi_2Te_3-to-HPMC mass ratio of 10:1) delivering the highest Seebeck coefficient. In contrast, the n-type Bi_2Te_3/HPMC@paper shows a negative S and follows a similar composition-dependent trend. We further evaluated the influence of the Bi_2Te_3/HPMC ratio on the electrical conductivity of Bi_2Te_3/HPMC@paper. The conductivity varies markedly with Bi_2Te_3 content: Increasing the Bi_2Te_3 fraction enhances the number of conductive pathways within the composite, thereby improving σ. However, an excessive Bi_2Te_3 loading leads to insufficient interparticle connectivity between adjacent Bi_2Te_3 grains, resulting in a decrease in σ, indicating that HPMC acts as a binder that bridges neighboring Bi_2Te_3 particles. BTHP-10 exhibits the highest conductivity, with σ values of 34.30 $S{\cdot}m^{-1}$ for the p-type and 18.20 $S{\cdot}m^{-1}$ for the n-type Bi_2Te_3/HPMC@paper. The maximum PF values of the p-type and n-type Bi_2Te_3/HPMC@paper reach 1.15 and 0.96 $\mu W{\cdot}m^{-1}{\cdot}K^{-2}$, respectively. Therefore, BTHP-10 was selected for subsequent experiments. The measured thermoelectric output under different temperature differences demonstrates that the open-circuit voltage (U_{OC}) and short-circuit current (I_{SC}) of both p-type and n-type Bi_2Te_3/HPMC@paper increase linearly with ΔT. At ΔT = 57.8 K, the p-type film exhibits an open-circuit voltage of 10.6 mV and a current of 23.5 μA (Figs. S5(a)–S5(c) in the ESM), while the n-type film shows −13.3 mV and −13.2 μA at ΔT = 56.9 K (Figs. S6(a)–S6(c) in the ESM). The Seebeck coefficients derived from linear fitting are +182.96 $\mu V{\cdot}K^{-1}$ (p-type) and −229.98 $\mu V{\cdot}K^{-1}$ (n-type) (Figs. 2(a) and 2(b)), indicating stable and reliable thermoelectric behavior for both films. Figure S7 in the ESM shows the variation of areal power density of the p-type and n-type Bi_2Te_3/HPMC@paper under different temperature differences. As ΔT increases, the areal power density of both films rises continuously. The p-type film delivers an areal power density of 1.71 $nW{\cdot}cm^{-2}$ at ΔT = 57.9 K, whereas the n-type film reaches a markedly higher value of 11.28 $nW{\cdot}cm^{-2}$ at ΔT = 50.7 K. These results indicate that, under comparable thermal driving, the n-type film exhibits a higher power output per unit area, and both films demonstrate enhanced power generation with increasing ΔT. As shown in Table S2 in the ESM, the performance comparison between the thermoelectric composite films obtained in this study and those previously reported in the literature demonstrates that the Bi_2Te_3/HPMC@paper prepared in this work exhibits a superior Seebeck coefficient compared with previously reported thermoelectric films [23, 41–44]. This high performance can be attributed to the topological properties of Bi_2Te_3, which significantly enhance the mobility of charge carriers, thereby improving its thermoelectric performance. When combined with the HPMC matrix, it not only imparts excellent mechanical flexibility and conformability to the material but also promotes efficient carrier transport. As a result, the material maintains high thermoelectric efficiency while providing the flexibility required for wearable applications. The flexibility of the Bi_2Te_3/HPMC@paper was verified by 180° cyclic bending tests (Fig. 2(c)). After 300 cyclic bending cycles, the relative resistance change of the p-type and n-type Bi_2Te_3/HPMC@paper shows no significant increase, rising by only 17.6% and 19.6%, respectively, demonstrating their good structural integrity and electrical stability (Figs. S8 in the ESM). To evaluate the thermoelectric output under biologically relevant small temperature differences, we measured the open-circuit voltage of individual p-type and n-type Bi_2Te_3/HPMC@paper films (Figs. S9 in the ESM). For the p-type film, the output voltage (U) increases from 0.22 mV at ΔT = 1 K to 0.60 mV at 3 K and 1.1 mV at 5 K. Correspondingly, the n-type film delivers voltages of −0.28, −0.64, and −1.2 mV at ΔT = 1, 3, and 5 K, respectively. In this low ΔT regime, the voltage rises monotonically with increasing ΔT, indicating a stable Seebeck response and demonstrating that measurable power-generation outputs can be achieved even under small thermal driving forces. To further evaluate thermoelectric performance, the Bi_2Te_3/HPMC@paper were connected in series with different external load resistances (R_L), and the corresponding relationships between U and output power (P_{out}) were obtained. According to the thermoelectric output model, the power output can be expressed as [27, 45]: $P_{out} = I^2 R_L = \frac{U_{OC}^2 \times R_L}{(R_i - R_L)^2 + 4R_i R_L}$, where R_i and R_L represent the internal and load resistances of the film, respectively. When $R_L = R_i$, the power reaches its maximum value: $P_{out,max} = \frac{U_{OC}^2}{4R_i}$ [46]. The current–voltage (I–V) curves of the

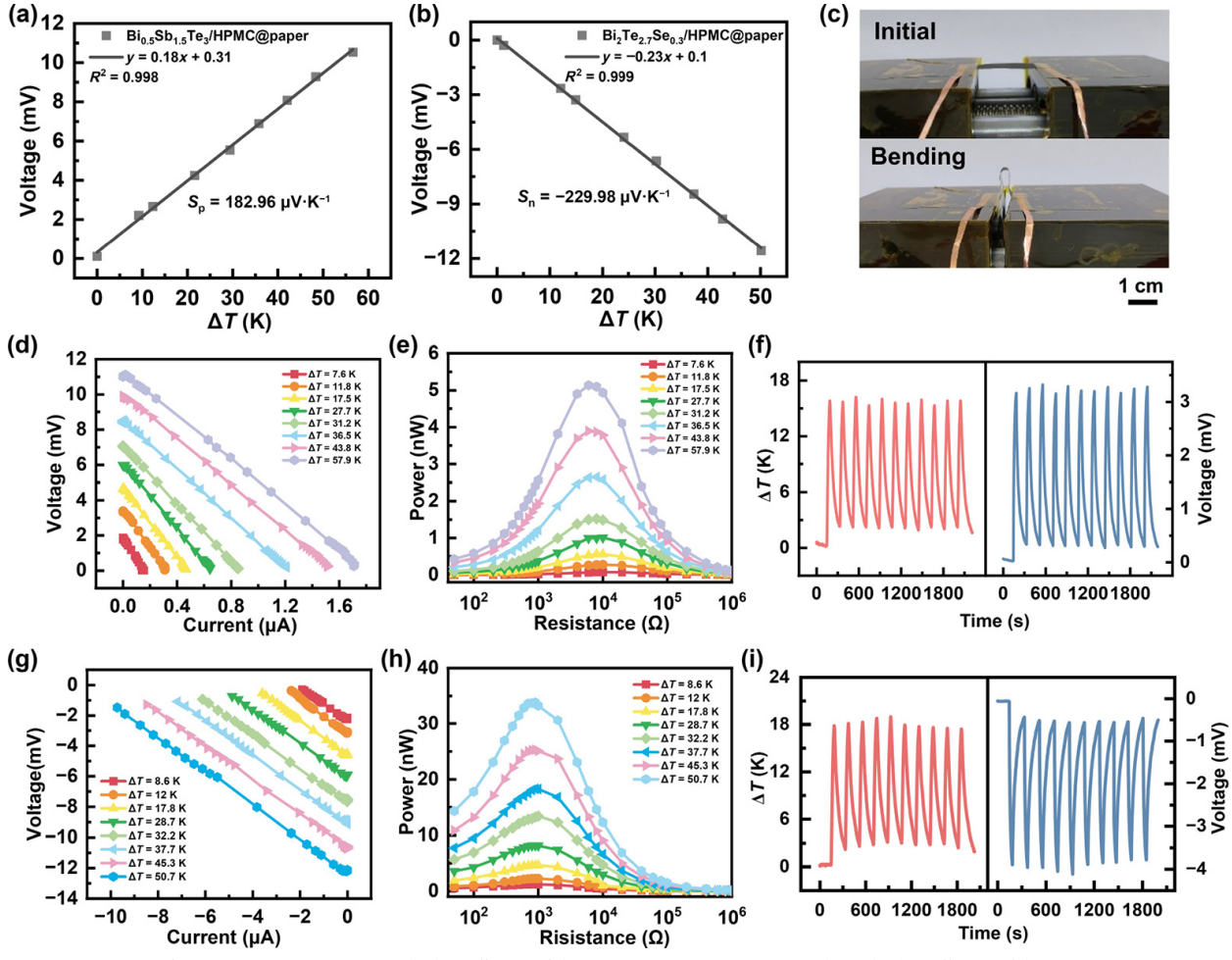

Figure 2 TE properties of Bi_2Te_3/HPMC@paper. (a) Seebeck coefficient of the p-type Bi_2Te_3/HPMC@paper. (b) Seebeck coefficient of the n-type Bi_2Te_3/HPMC@paper. (c) Optical photograph of a Bi_2Te_3/HPMC@paper under a bending state. (d) *I*–*V* curves of individual p-type Bi_2Te_3/HPMC@paper. (e) P_{out}–R_L curves of individual p-type Bi_2Te_3/HPMC@paper. (f) ΔT and output voltage of p-type Bi_2Te_3/HPMC@paper under repeated heating–cooling cycles. (g) *I*–*V* curves of individual n-type Bi_2Te_3/HPMC@paper. (h) P_{out}–R_L curves of individual n-type Bi_2Te_3/HPMC@paper. (i) ΔT and output voltage of n-type Bi_2Te_3/HPMC@paper under repeated heating–cooling cycles.

independent p-type and n-type Bi_2Te_3/HPMC@paper (Figs. 2(d) and 2(g)) exhibit excellent linearity, demonstrating good Ohmic contact between the composite films and copper electrodes. As ΔT increases from 7.6 to 57.9 K, the p-type film's open-circuit voltage rises from 1.9 to 11.0 mV, and the short-circuit current increases from 0.2 to 1.7 μA. Similarly, the n-type film exhibits an open-circuit voltage change from −2.1 to −12.1 mV, with the short-circuit current increasing from −1.9 to −9.7 μA. Based on these measurements, the p-type film achieves a maximum power output of 5.1 nW at ΔT = 57.9 K, whereas the n-type film reaches 33.8 nW at ΔT = 50.7 K (Figs. 2(e) and 2(h)), confirming excellent power-generation capability. Under repeated heating–cooling cycles, the Bi_2Te_3/HPMC@paper exhibit stable and reproducible voltage and current responses (Figs. S10 and S11 in the ESM). At ΔT = 15.8 K, the p-type film generates a steady voltage of approximately 3.4 mV (Fig. 2(f)), while the n-type film outputs −3.9 mV at ΔT = 18.2 K (Fig. 2(i)). The minimal signal fluctuation during multiple cycles indicates outstanding thermal stability and repeatability of the composite system. Overall, the Bi_2Te_3/HPMC@paper simultaneously achieves high Seebeck coefficients and excellent flexibility, exhibiting stable thermoelectric response and mechanical durability, thereby establishing a solid foundation for the development of next-generation flexible thermoelectric energy-conversion devices.

2.3 Performances of Bi_2Te_3/HPMC@paper TEGs based on a planar structure

The fundamental operating principle of a TEG is to directly convert thermal energy into electrical energy through a series circuit formed by alternately connecting n-type and p-type thermoelectric legs [3]. In flexible and wearable applications, the planar configuration is considered an ideal design for compact thermal energy harvesting due to its mechanical simplicity and high spatial utilization efficiency [47, 48]. In this structure, the thermoelectric legs are aligned parallel to the substrate, allowing seamless integration with flexible supports while maintaining mechanical stability and deformation adaptability. In this study, a planar Bi_2Te_3/HPMC@paper TEG was constructed on a polyimide (PI) substrate, which provides excellent chemical and thermal stability (Fig. 3(a)). The finished device is shown in Fig. S12 in the ESM, demonstrating good flexibility and bendability. For assembled TEG devices, $S_{device} = \frac{dV}{d\Delta T}$, which is extracted from the slope of the *V*–ΔT curve. S_{device} is a system-level metric governed by the series integration of

thermoelectric units and should be distinguished from the intrinsic Seebeck coefficients of the constituent p-type and n-type films. Initially, a flexible thermoelectric generator comprising a single p–n pair (denoted as TEG-1pn) was fabricated for performance evaluation. As shown in Fig. 3(b), the output voltage of TEG-1pn increases linearly with the ΔT from 7.8 to 45.2 K, reaching 17.1 mV at ΔT = 30.8 K, corresponding to S_{device} = 551.26 μV·K^{-1}. The I–V curves (Fig. 3(c)) exhibit excellent linearity, indicating good Ohmic contact behavior. With increasing ΔT, both the open-circuit voltage and short-circuit current rise proportionally, and the maximum output power reaches 18.5 nW at ΔT = 45.2 K (Fig. 3(d)). Repeated heating-cooling cycle tests (Fig. S13 in the ESM) show that TEG-1pn maintains a stable output voltage of approximately 8.9 mV under ΔT = 20.1 K, with negligible fluctuation, confirming outstanding cyclic stability. Since the power output of a single p–n pair is limited, the output performance was further enhanced by serial integration. Devices consisting of two p–n pairs (TEG-2pn) and three p–n pairs (TEG-3pn) were fabricated (Figs. 3(e)–3(j)). The output voltage of TEG-2pn increases linearly with ΔT, reaching 38.3 mV at ΔT = 42.4 K, corresponding to S_{device} = 909.96 μV·K^{-1}; the maximum power output reaches 47.8 nW at ΔT = 49.4 K. Further increasing the number of serially connected units, TEG-3pn delivers an open-circuit voltage as high as 62.6 mV at ΔT = 57.9 K, with S_{device} = 1274.54 μV·K^{-1} and a maximum output power of

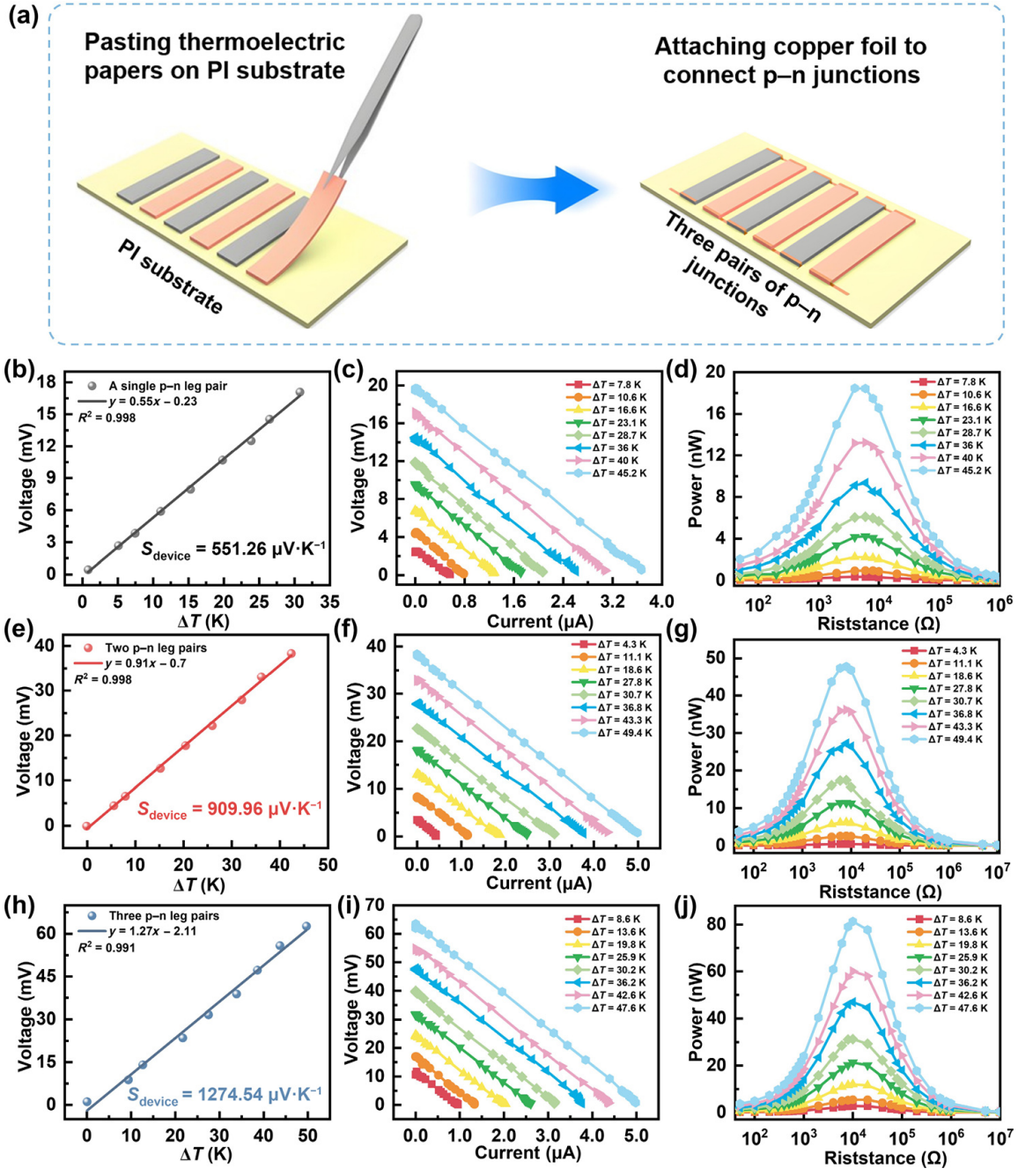

Figure 3 Performances of Bi_2Te_3/HPMC@paper TEGs based on a planar structure. (a) Schematic illustration of the Bi_2Te_3/HPMC@paper TEG assembly. (b) S_{device} of TEG-1pn. (c) I–V characteristics of TEG-1pn. (d) P_{out}–R_L curves of TEG-1pn. (e) S_{device} for TEG-2pn. (f) I–V characteristics of TEG-2pn. (g) P_{out}–R_L curves of TEG-2pn. (h) S_{device} for TEG-3pn. (i) I–V characteristics of TEG-3pn. (j) P_{out}–R_L curves of TEG-3pn.

81.3 nW (Fig. 3(j)). Cyclic tests further demonstrate that the multi-pair serial devices maintain stable output performance under repeated thermal excitation (Fig. S14 in the ESM). For example, TEG-3pn outputs a steady voltage of approximately 22.8 mV at ΔT = 16.9 K with negligible signal attenuation (Fig. S15 in the ESM), confirming its excellent reliability and long-term operational stability. In summary, the Bi_2Te_3/HPMC@paper-based planar TEG effectively enhances thermoelectric output and energy conversion efficiency through a multi-pair serial-connection strategy, while retaining excellent mechanical flexibility and cyclic durability. This work provides a viable structural paradigm for the development of highly integrated flexible thermoelectric energy-harvesting systems.

2.4 Performances of Bi_2Te_3/HPMC@paper TEGs based on a stacked architecture

To further enhance energy conversion efficiency and fully exploit vertical temperature differences, a stacked-architecture TEG was designed in this study. Compared with conventional planar configurations, the stacked architecture enables more effective vertical heat harvesting, allowing efficient energy capture from nonplanar or curved heat sources [49]. Through this structural optimization strategy, the device not only improves temperature gradient utilization but also maintains stable output performance under bending conditions. Based on the previously developed high-performance p-type and n-type Bi_2Te_3/HPMC@paper, a multilevel stacked thermoelectric generator was constructed (Fig. 4(a)). The optical photograph of the TEG based on the stacked structure is shown in Fig. S16 in the ESM. The Level-I structure, consisting of a single p–n pair connected in series, was first fabricated to evaluate the fundamental thermoelectric performance. As shown in Fig. 4(b), the output voltage increases linearly with the ΔT. At ΔT = 54.9 K, the Level-I TEG delivers an output voltage of 22.4 mV, corresponding to S_{device} = 408.86 μV·K^{-1}. The I–V curves (Fig. 4(c)) exhibit a good linear relationship, indicating stable electrode contact. The P_{out}–R_L curves (Fig. 4(d)) show that the maximum output power reaches 25.6 nW at ΔT = 57.9 K. Repeated heating–cooling cycle tests (Fig. S17 in the ESM) demonstrate stable voltage output (~ 6.6 mV at ΔT = 16.1 K) with negligible fluctuation, suggesting excellent thermal response and cyclic stability. To further enhance the output capability, multiple units were serially integrated. The Level-II structure was assembled by stacking three Level-I units in series, while the Level-III structure was built by serially connecting five Level-II units (Fig. 4(a)). The output characteristics of the Level-II TEG (Figs. 4(e)–4(g)) show a linear increase in voltage with ΔT, reaching 29.4 mV at ΔT = 23.2 K, corresponding to S_{device} = 1273.66 μV·K^{-1}, and a maximum power output of 88.0 nW. Cyclic testing reveals stable voltage output of ~ 26.1 mV under ΔT = 9.4 K (Fig. S18 in the ESM), confirming excellent reproducibility. The Level-III stacked device exhibits even higher output performance (Figs. 4(h)–4(j)), delivering an open-circuit voltage of 178.2 mV at ΔT = 27.0 K with S_{device} = 6659.13 μV·K^{-1}. The I–V characteristics remain linear, indicating good internal resistance matching. At ΔT = 28.3 K, the maximum power reaches 61.8 nW. Reproducibility testing (Fig. S19 in the ESM) shows that the output voltage remains stable at ~ 54.9 mV under ΔT = 7.9 K, without noticeable degradation, confirming excellent electrical stability during multiple thermal cycles. Overall, the Bi_2Te_3/HPMC@paper-based stacked TEG significantly enhances temperature-gradient utilization and power density through hierarchical serial integration, while maintaining excellent flexibility and structural integrity. This architecture effectively balances high energy conversion efficiency and mechanical compliance, providing a promising design strategy for developing high-power-output, flexible electronic systems.

To overcome the limited active area and low output power of individual thermoelectric units, a Level-III TEG based on multi-unit integration was developed to achieve higher energy output and enhanced wearability (Fig. S20(a) in the ESM). Infrared thermography (Fig. S20(b) in the ESM) revealed a clear temperature difference between the top and bottom surfaces of the TEG, confirming its strong heat-capturing and thermal-conduction capability. As the ΔT increased, both output voltage and current exhibited a linear rise (Figs. S21(a)–S21(c) in the ESM). At ΔT = 49.6 K, the TEG achieved a maximum open-circuit voltage of 555.2 mV and an output current of 5.9 μA, corresponding to S_{device} = 11,330.25 μV·K^{-1} (Fig. S22(a) in the ESM). This ultrahigh S_{device} mainly arises from voltage accumulation enabled by series integration within the stacked architecture, representing a system-level metric rather than an intrinsic material property. When ΔT increased from 5.6 to 49.6 K, the open-circuit voltage rose from 72.2 to 477.1 mV, while the short-circuit current increased from 0.7 to 5.3 μA (Fig. S22(b) in the ESM), demonstrating a well-defined linear thermoelectric response. The power output results (Fig. S22(c) in the ESM) show that the maximum output power increased significantly with ΔT, reaching 617.4 nW at ΔT = 49.6 K. Compared with lower-order TEG structures, the Level-III configuration exhibited markedly higher power density, indicating that the combined multilevel stacking and flexible encapsulation strategies effectively enhanced energy-harvesting efficiency. This vertically oriented stacked design enables the thermoelectric units to fully exploit the temperature difference of skin or nonplanar heat sources, achieving efficient heat collection. Meanwhile, the elastic structure of the Ecoflex supporting layer imparts exceptional mechanical compliance and fatigue resistance, allowing the device to maintain stable output performance under large temperature differences and repeated bending cycles. In summary, the Level-III TEG achieves high output power and excellent operational stability through structural optimization, combining superior flexibility with efficient energy conversion. This work provides a practical and scalable design strategy for developing high-power-density, flexible electronic systems.

2.5 Applications of the f-TEGs

Although the multilevel stacked TEGs (Level-II and Level-III) exhibited superior output performance, the stacked configuration already met the essential requirements for flexible and wearable devices, such as mechanical robustness and efficient utilization of vertical temperature differences. For practical demonstration, a simplified Level-I structure based on the same Bi_2Te_3/HPMC@paper thermoelectric units was adopted. This design maintains the same material system and thermoelectric working principle as the stacked architecture, while offering greater flexibility, reduced thickness, and better conformity to curved or skin surfaces. The Level-I device thus serves as a representative prototype to validate the mechanical stability, durability, and body-heat energy-harvesting capability of the proposed flexible TEG system. To further verify the practical applicability of this flexible TEG design in real-world wearable scenarios, a larger-area f-TEG composed of ten serially connected Level-I units was fabricated.

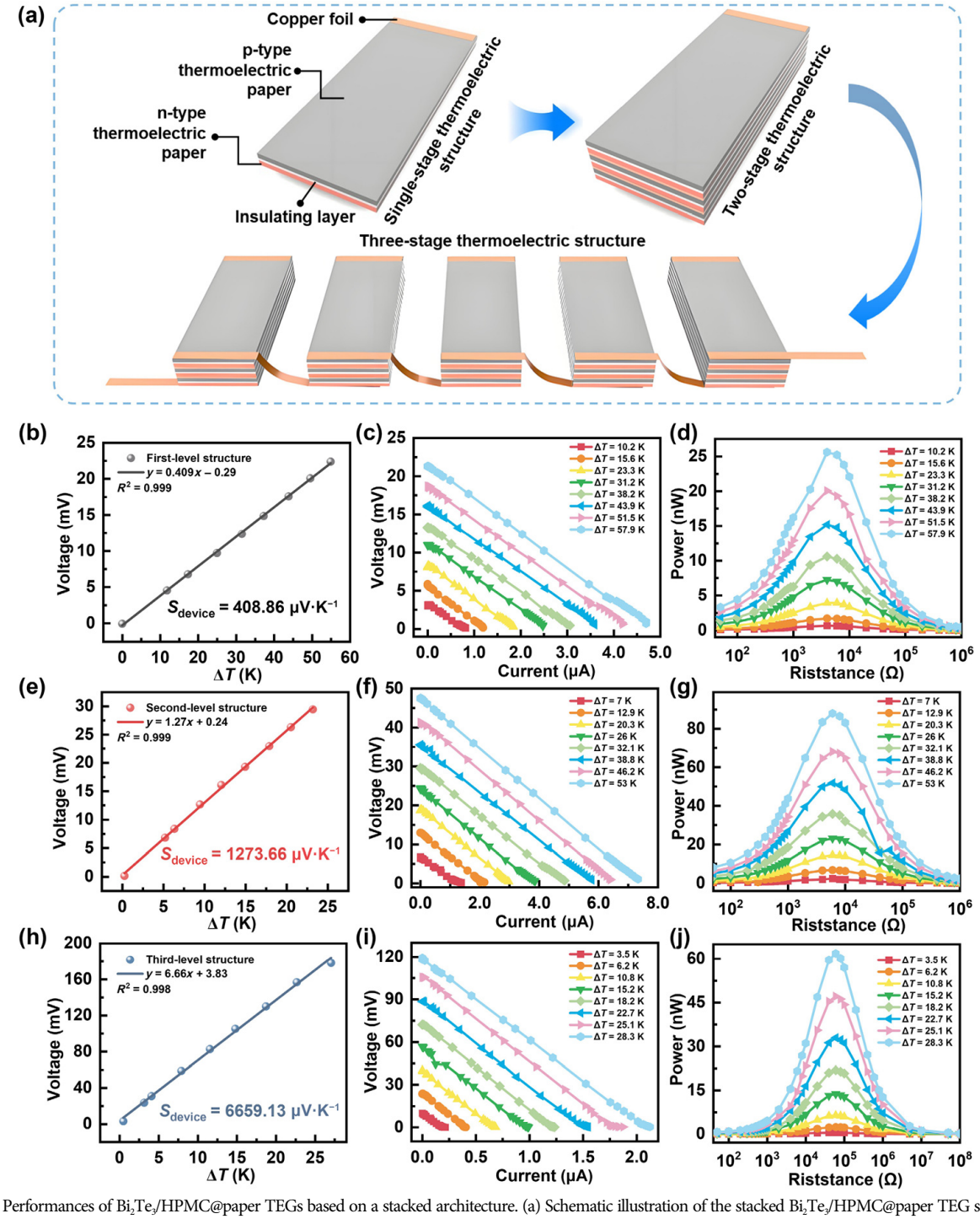

Figure 4 Performances of Bi_2Te_3/HPMC@paper TEGs based on a stacked architecture. (a) Schematic illustration of the stacked Bi_2Te_3/HPMC@paper TEG structure. (b) S_{device} for the Level-I TEG. (c) *I*–*V* characteristics of the Level-I TEG. (d) P_{out}–R_L curves of the Level-I TEG. (e) S_{device} for the Level-II TEG. (f) *I*–*V* characteristics of the Level-II TEG. (g) P_{out}–R_L curves of the Level-II TEG. (h) S_{device} for the Level-III TEG. (i) *I*–*V* characteristics of the Level-III TEG. (j) P_{out}–R_L curves of the Level-III TEG.

The device employed Cu electrodes for electrical interconnection and was uniformly embedded within an Ecoflex flexible substrate to achieve excellent mechanical compliance and conformability to the human body. Figure 5(a) shows the schematic illustration of the assembly process for the Level-I f-TEG. As shown in Figs. 5(b)–5(d), the f-TEG can accommodate various deformation states, including flat, twisted, and bent configurations, exhibiting excellent flexibility and mechanical adaptability. Airflow-sensitivity testing revealed that the device effectively dissipated heat through lateral air convection while producing voltage responses to airflow fluctuations, enabling real-time wind-speed sensing capability (Fig. 5(e)). Flexibility and structural stability are critical factors in ensuring continuous power output of thermoelectric generators [50–53]. For wearable energy harvesting applications, stable thermal contact between the device and complex curved surfaces is essential for efficient energy conversion [54–57]. As illustrated in Fig. 5(f), the Level-I f-TEG can be comfortably worn on the wrist, conforming well to the curvature of human skin and maintaining

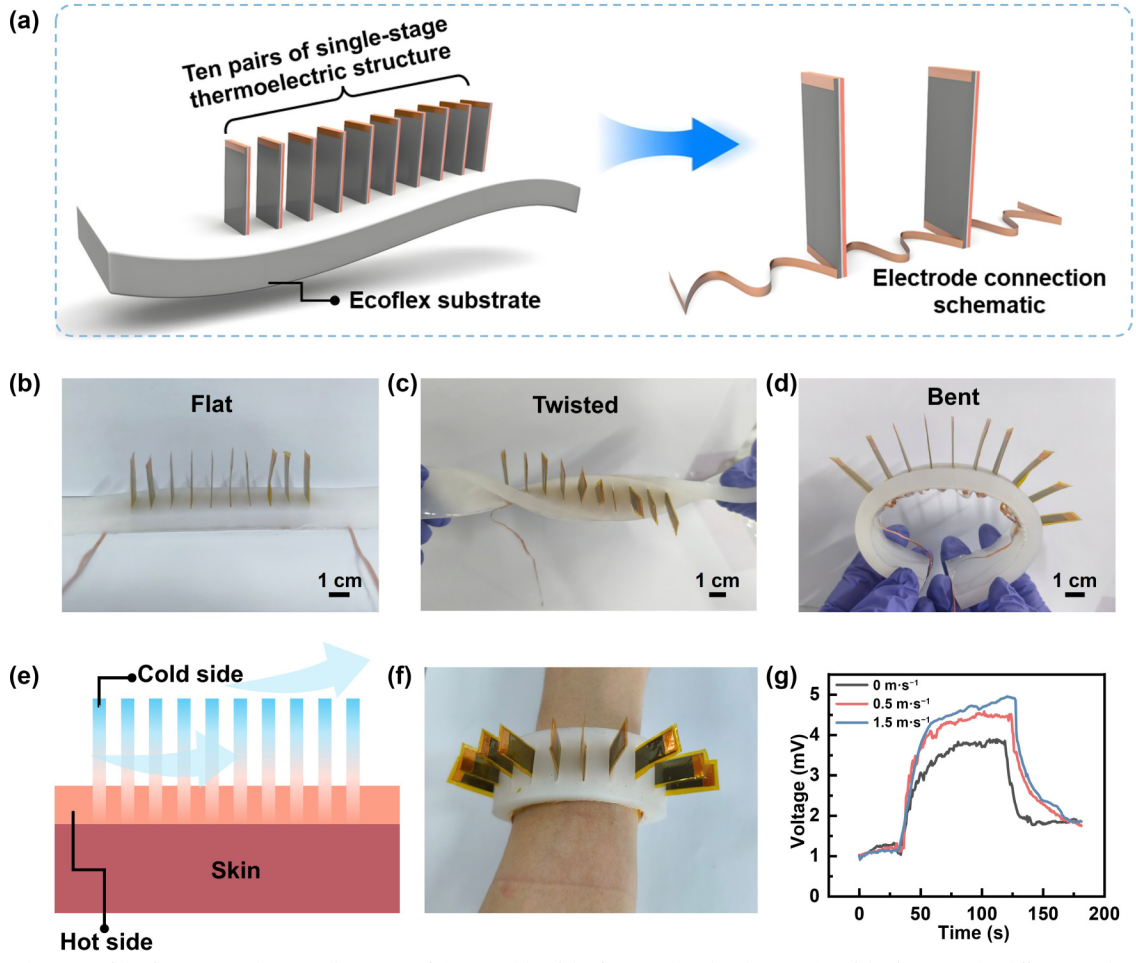

Figure 5 Applications of the f-TEG. (a) Schematic illustration of the assembly of the f-TEG. ((b)–(d)) Photographs of the f-TEG under different mechanical states: (b) flat, (c) twisted, and (d) bent. (e) Schematic diagram of airflow sensitivity under different wind speeds. (f) Photograph of the f-TEG worn on the wrist. (g) Output performance of the f-TEG at different wind speeds.

stable electrical output during daily motion, confirming excellent wearability and mechanical reliability. The performance of the f-TEG under different wind-speed conditions is shown in Fig. 5(g). In still air, the initial output voltage is approximately 1.1 mV. When worn on the wrist, the voltage rapidly increases to 3.9 mV due to the enhanced temperature difference between the skin and the surrounding environment, and returns to its baseline value after removal. As wind speed increases from 0.5 to 1.5 $m{\cdot}s^{-1}$, the output voltage rises linearly, reaching a maximum of 5.0 mV. This result indicates that convective heat dissipation induced by airflow can significantly enhance the power output and energy-transfer efficiency of the device. Overall, the Level-I f-TEG exhibits excellent flexibility, stability, and energy responsiveness under various mechanical deformations and environmental conditions. The device conforms well to the human body surface and shows great potential for wearable energy-harvesting and environmental-sensing applications.

The greatest advantage of the f-TEG lies in its ability to conform intimately to nonplanar surfaces, enabling efficient harvesting of body-surface waste heat and stable thermoelectric signal generation while adapting to diverse human geometries and motion-induced deformations. To demonstrate the practical potential of Bi_2Te_3/HPMC@paper in wearable energy systems, a smart wristband was constructed (Fig. 6(a)). The device integrates four p–n leg pairs, which are connected in series using copper foils and conductive silver paste to minimize interfacial resistance (Fig. S23 in the ESM). The thermoelectric module was then embedded in the inner side of a fabric wristband, forming a flexible thermoelectric wristband (Fig. 6(b)). The voltage amplifier used in this work is a commercially available module (AD620, Shenzhen Colibri Technologies Co., Ltd.), offering a maximum gain of up to 10,000. The minimum operating voltage of the amplifier is 3 V. As shown in Fig. S24 in the ESM, its internal circuitry mainly consists of a power-supply module, an input module, and an output module. In our smart wristband design, the power-supply module of the amplifier is powered by two series-connected 1.5 V alkaline coin-cell batteries, whereas the voltage generated by the thermoelectric device is fed into the input module and amplified by the commercial amplifier to drive the pedometer. In its initial state, the pedometer remains unpowered. Once the wristband is worn, a stable temperature difference forms between the skin and ambient air, driving an immediate voltage output via the Seebeck effect (Fig. S25 in the ESM). The voltage signal was amplified to above 3 V using the AD620 module, thereby enabling continuous operation of the integrated pedometer (model AU-313) (Fig. 6(c)(i)). When the wearer begins walking, the pedometer enables real-time step counting (Fig. 6(c)(ii)). After restarting the pedometer, the system continued to operate steadily and accurately (Fig. 6(c)(iii)),

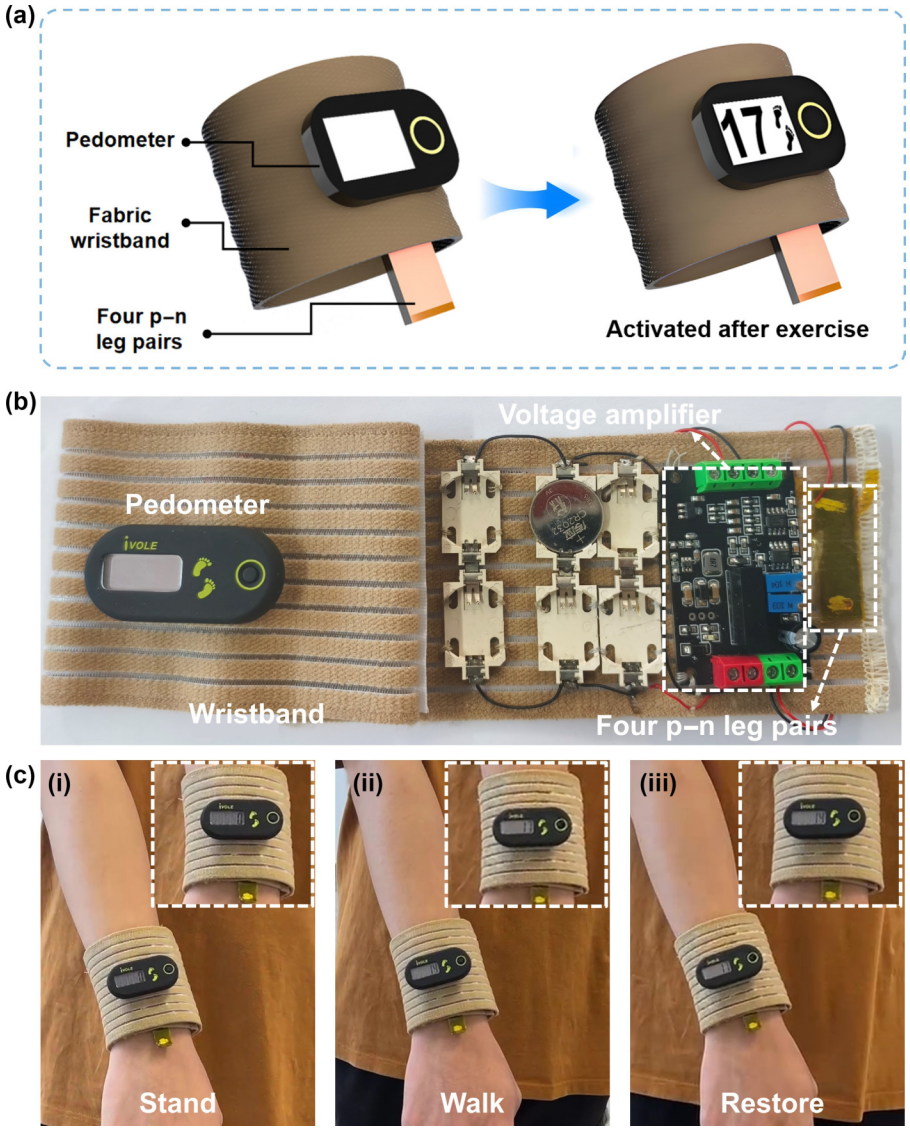

Figure 6 Smart wristband. (a) Schematic illustration of the smart wristband. (b) Optical photograph of the smart wristband. (c) Optical photographs illustrating a volunteer wearing the wristband while standing, walking, and walking after restarting the pedometer, accompanied by magnified views of the pedometer display.

indicating good signal continuity and operational stability. Movie S1 in the ESM shows the working process of the smart wristband. Overall, this demonstration verifies the feasibility of integrating Bi_2Te_3/HPMC@paper into wearable platforms for conformal body-surface heat harvesting and thermoelectric signal generation, and further highlights the potential of flexible thermoelectric devices for future wearable sensing and health-monitoring systems.

3 Conclusions

This work proposes a design strategy for high-performance flexible Bi_2Te_3/HPMC@paper and its multilevel stacked TEGs. The Bi_2Te_3/HPMC@paper fabricated via a vacuum filtration method exhibit a well-balanced combination of excellent thermoelectric performance and mechanical flexibility, achieving simultaneous optimization of flexibility and energy output. The introduction of a hierarchical stacked architecture effectively enhances temperature difference utilization and energy conversion capability. Among them, the Level-III f-TEG delivers an open-circuit voltage of 555.2 mV and a maximum output power of 617.4 nW, demonstrating outstanding energy-harvesting capacity and operational stability. When integrated with an Ecoflex flexible substrate, the device maintains stable output under various mechanical deformation conditions, exhibiting superior conformability and durability. Furthermore, the smart wristband developed in this study harnesses body heat to provide a continuous power supply for low-power wearable electronics. Overall, this work establishes a wearable and readily integrable flexible thermoelectric energy system with broad prospects in wearable thermoelectric energy-harvesting electronics and intelligent wearable devices, and it offers new insights for the design of next-generation flexible and sustainable energy-harvesting systems.

Electronic Supplementary Material: Supplementary material (including experimental details, fabrication and characterization of Bi_2Te_3/HPMC@paper films and TEG devices, thermoelectric performance and stability tests, and supplementary information on the smart wristband demonstration) is available in the online version of this article at https://doi.org/10.26599/NR.2026.94908713.

Data availability

All data needed to support the conclusions in the paper are presented in the manuscript and the Electronic Supplementary Material. Additional data related to this paper may be requested from the corresponding author upon request.

Acknowledgements

This work was supported by the Fuzhou Major Science and Technology Project (No. 2025-ZD-010), the Natural Science Foundation of Fujian Province (No. 2025J01999), and the National Natural Science Foundation of China.

Declaration of competing interest

All the contributing authors report no conflict of interests in this work.

Author contribution statement

J. G. was responsible for conducting the experimental work and writing the manuscript. J. H. Z. assisted in drawing simulation figures and revising the manuscript. B. Z. Z. and W. Y. assisted in performing the experimental work. M. C. W., Q. H. G., Z. Q. L., and H. C. R. jointly participated in the discussion of the experimental results and reviewed the manuscript. All the authors have approved the final manuscript.

Use of AI statement

None.

References

[1] Wang, L. Q.; Li, A. R.; Wu, X. Z.; Li, J. K.; Ohsawa, T.; Mori, T. Active diffusion controlled dual stability in thermoelectrics for sustainable heat harvesting. *Adv. Mater.* **2025**, *37*, 2508270.

[2] Liu, K.; Wang, J. Y.; Pan, X. R.; Tian, S. Y.; Liu, Y. D.; Zhang, Z.; Di, Y. Q.; Chen, J. P.; Wu, C. W.; Deng, X. Y. et al. n-Type thermoelectric elastomers. *Nature* **2025**, *644*, 920–926.

[3] He, C. J.; Shi, X. L.; Li, N. H.; Li, M.; Pei, J.; Chen, Z. G. Ductile inorganic thermoelectrics: Advances, challenges, and perspectives. *Adv. Energy Mater.* **2025**, *15*, e03115.

[4] Wang, B. S.; Li, L.; Zhang, K. H.; Wu, X. H.; Yu, K. Enhanced thermoelectric system by dual-band radiative cooling for all-day energy harvesting. *Energy.* **2025**, *330*, 136994.

[5] Basit, A.; Xin, J. W.; Li, X.; Hussain, T.; Wang, G. Y.; Dai, J. Y.; Zheng, G. P. A review on high-performance flexible thermoelectrics: Material, device, and applications. *Microstructures* **2025**, *5*, 2025028.

[6] Weng, M. C.; Qiu, Y. H.; Zhou, J. H.; Feng, H. H.; Yi, N. Z.; Zuo, Y.; Chen, J. Y.; Zhou, P. D.; You, M. H.; Guo, Q. H. et al. Multi-functional $Nb_4C_3T_x$ (MXene)-bacterial cellulose composites for multimodal self-powered sensors toward a material/temperature recognition system. *Chem. Eng. J.* **2025**, *522*, 167607.

[7] Shi, X. F.; Li, Y. J.; Shi, N.; Ji, C. Y.; Hou, L.; Shi, Y. K.; Xu, J. Y.; Lan, Y. R.; Wei, Q. C.; Ma, G. L. et al. Phase transition driven tough hydrogel ionic thermoelectric cell with giant thermopower. *Nat. Commun.* **2025**, *16*, 9002.

[8] Jeong, Y. J.; Jung, J.; Suh, E. H.; Yun, D. J.; Oh, J. G.; Jang, J. Self-healable and stretchable organic thermoelectric materials: Electrically percolated polymer nanowires embedded in thermoplastic elastomer matrix. *Adv. Funct. Mater.* **2020**, *30*, 1905809.

[9] Fu, C. L.; Cheng, M. Y.; Hung, N. T.; Rha, E.; Chen, Z. T.; Okabe, R.; Carrizales, D. C.; Mandal, M.; Cheng, Y. Q.; Li, M. D. AI-driven defect engineering for advanced thermoelectric materials. *Adv. Mater.* **2025**, *37*, 2505642.

[10] Chen, J. X.; Ou, K. J.; Wu, Y. C.; Li, J. W.; Wang, J. H.; Kuo, C. F. J.; Cheng, C. C.; Tseng, Y. H.; Chiu, C. W. Highly compressible and efficient CNT/rGO/PDMS thermoelectric generator based on a 3D sponge-structured network for harvesting energy from a shoe sole. *ACS Appl. Electron. Mater.* **2025**, *7*, 1871–1882.

[11] Li, J. J.; He, X. Y.; Wang, J. H.; Zhu, S. Y.; Zhang, M. C.; Wu, C. X.; Dong, G. Y.; Liu, R. H.; Wang, L. M.; Chen, L. D. et al. Nanoarchitectonics of high-performance and flexible n-type organic–inorganic composite thermoelectric fibers for wearable electronics. *ACS Nano* **2025**, *19*, 11440–11449.

[12] Dai, Z. Y.; Lei, M.; Ding, S.; Zhou, Q.; Ji, B.; Wang, M. R.; Zhou, B. P. Durable superhydrophobic surface in wearable sensors: From nature to application. *Exploration* **2024**, *4*, 20230046.

[13] Lv, W. Q.; Tang, W. X.; Yu, P. L.; Kainat, J.; Zhou, Z. F.; Lan, J. L.; Yang, X. P.; Lin, Y. H. Polymorphic Interface engineering for high-performance Ag_2Se-based flexible thermoelectric device. *J. Colloid Interface Sci.* **2025**, *699*, 138307.

[14] Li, M. J.; Wu, L. X.; Zheng, G.; Zhang, X. L.; Liang, Z.; Liu, M. N.; Li, R.; Zhang, J.; Long, Y. Z. Flexible piezoelectric-thermoelectric coupled nanofiber generator for self-powered multimodal sensing system. *Adv. Funct. Mater.* **2026**, *36*, e16438.

[15] Guo, Q. H.; Guo, J.; Zhou, J. H.; Yu, W.; Zhou, P. D.; Yang, K. H.; Zheng, C.; Zeng, S. F.; Hua, N. B.; You, M. H. et al. Patternable and flexible thermoelectric generators based on Bi_2Te_3/silk fibroin composites for temperature sensing and wearable applications. *Chem. Eng. J.* **2024**, *500*, 157077.

[16] Mao, D. S.; Yang, J. M.; Han, M.; Huang, X. G.; Wang, J. R.; Jia, B. H.; Wang, Z. B.; Xu, X.; Xie, L.; Zhou, Y. et al. Homo-layer flexible Bi_2Te_3-based films with high thermoelectric performance. *Sci. Adv.* **2025**, *11*, eadz1019.

[17] Wei, R. X.; Cui, X. J.; Khan, S. A.; Bai, C. H.; Wang, C. J.; Zhang, J.; Hao, R. F.; Huang, Z. Q.; Li, Z.; Zhang, H. L. Self-powered versatile on-hand virtual interface enabled by thermogalvanic hydrogel. *Chem. Eng. J.* **2025**, *522*, 167739.

[18] Li, N.; Wang, Z. S.; Yang, X. R.; Zhang, Z. Y.; Zhang, W. D.; Sang, S. B.; Zhang, H. L. Deep-learning-assisted thermogalvanic hydrogel E-skin for self-powered signature recognition and biometric authentication. *Adv. Funct. Mater.* **2024**, *34*, 2314419.

[19] Li, N.; Wang, Z. S.; Niu, Y.; Li, Y.; Wen, S. Y.; Zhang, H. L.; Lin, Z. H. Bionic multimodal augmented somatosensory receptor enabled by thermogalvanic hydrogel. *Adv. Sci.* **2025**, *12*, e05873.

[20] Zhu, P. C.; Shi, C. Q.; Wang, Y. L.; Wang, Y. L.; Yu, Y. D.; Wang, Y.; Deng, Y.; Xiao, J. L. Recyclable, healable, and stretchable high-power thermoelectric generator. *Adv. Energy Mater.* **2021**, *11*, 2100920.

[21] Sun, Z. Y.; Ou, Q. D.; Dong, C.; Zhou, J. S.; Hu, H. Y.; Li, C.; Huang, Z. D. Conducting polymer hydrogels based on supramolecular strategies for wearable sensors. *Exploration* **2024**, *4*, 20220167.

[22] Liu, H. H.; Jin, X. S.; Xu, Q.; Jin, Y. M.; Zhang, X.; Lv, S. L. Integrated hydrogel-based photothermoelectric device for energy harvesting. *ACS Appl. Mater. Interfaces* **2025**, *17*, 36943–36950.

[23] Fan, W. J.; Yin, Q.; Wang, Q.; Wan, Z. L.; Nie, L.; Ye, Q. M.; Li, J.; Huang, J. S.; Xu, J. K. All-3D-printed PEDOT:PSS-based stretchable thermoelectric devices for power generation. *ACS Appl. Mater. Interfaces* **2025**, *17*, 40836–40844.

[24] Hu, K.; Yang, D. W.; Hui, Y. Y.; Zhang, H. Z.; Song, R. G.; Liu, Y. T.; Wang, J.; Wen, P.; He, D. P.; Liu, X. P. et al. Optimized thermal design for excellent wearable thermoelectric generator. *J. Mater. Chem. A* **2022**, *10*, 24985–24994.

[25] Ding, Q. F.; Li, Z. Y.; Hou, Y.; Li, C.; Sun, X. L.; Zhu, Z.; Zhou, W. J.; Wu, Z. H.; Yan, X. X.; Liu, R. M. et al. 3D-Printing assisted bidirectional π-structured thermoelectric generators: Reverse-designed flexible architectures for curved heat sources. *Adv. Mater.* **2026**, *38*, e11872.

[26] Wang, D. Y.; Ding, J. M.; Ma, Y. Q.; Xu, C. L.; Li, Z. Y.; Zhang, X.; Zhao, Y.; Zhao, Y.; Di, Y. Q.; Liu, L. Y. et al. Multi-heterojunctioned

plastics with high thermoelectric figure of merit. *Nature* **2024**, *632*, 528–535.
[27] Liang, L. R.; Li, L. W.; Liu, L.; Dong, S. Y.; Du, C. Y.; Ye, Z. Q.; Chen, G. M. A compressible wave-like thermoelectric generator with excellent mechanical and humidity stability. *Chem. Eng. J.* **2025**, *519*, 165185.
[28] Xia, B. J.; Shi, X. L.; Zhang, L.; Luo, J.; Chen, W. Y.; Hu, B. X.; Cao, T. Y.; Wu, T.; Liu, W. D.; Yang, Y. L. et al. Vertically designed high-performance and flexible thermoelectric generator based on optimized PEDOT:PSS/SWCNTs composite films. *Chem. Eng. J.* **2024**, *486*, 150305.
[29] Cao, T. Y.; Shi, X. L.; Chen, Z. G. Advances in the design and assembly of flexible thermoelectric device. *Prog. Mater. Sci.* **2023**, *131*, 101003.
[30] Kim, S.; Na, Y. J.; Nam, C.; Jeong, C. K.; Kim, K. T.; Park, K. I. Highly tailorable, ultra-foldable, and resorbable thermoelectric paper for origami-enabled energy generation. *Nano Energy* **2022**, *103*, 107824.
[31] Yan, H. T.; Gu, H. N.; Lu, S. Z.; Meng, F. J.; Ma, Q. L.; Xing, X.; Pan, S. H.; Che, Y. J. Bioinspired multifunctional conductive hydrogel based on hydroxypropyl methyl cellulose for flexible sensors. *Carbohydr. Polym.* **2025**, *368*, 124192.
[32] Li, X.; Liu, Z. G.; Hu, Z. Z.; Zhang, Y. P.; Zhou, Q.; Zhang, X. Y.; Zhang, T. Ultrabroadband, self-powered, highly-sensitive photodetector based on Bi_2Te_3/graphene heterostructure synergistically enhanced with photothermal mechanisms and Au antenna. *Adv. Funct. Mater.* **2026**, *36*, e12087.
[33] Deng, T. T.; Gao, Z. Q.; Li, Z.; Qiu, P. F.; Li, Z.; Yuan, X. J.; Ming, C.; Wei, T. R.; Chen, L. D.; Shi, X. Room-temperature exceptional plasticity in defective Bi_2Te_3-based bulk thermoelectric crystals. *Science* **2024**, *386*, 1112–1117.
[34] Li, L.; Shi, N. Q.; Jiang, X. Q.; Chen, W. P.; Ban, C. C.; Hao, J. D. Flexible thermoelectric films based on Bi_2Te_3 nanowires and boron nitride nanotube networks with carbon doping. *ACS Appl. Mater. Interfaces* **2023**, *15*, 31812–31823.
[35] Dong, G. Y.; Feng, J. H.; Qiu, G. J.; Yang, Y. X.; Chen, Q. Y.; Xiong, Y.; Wu, H. J.; Ling, Y. F.; Xi, L. L.; Long, C. et al. Oriented Bi_2Te_3-based films enabled high performance planar thermoelectric cooling device for hot spot elimination. *Nat. Commun.* **2024**, *15*, 9695.
[36] Chen, W. Y.; Shi, X. L.; Li, M.; Liu, T.; Mao, Y. Q.; Liu, Q. Y.; Dargusch, M.; Zou, J.; Lu, G. Q.; Chen, Z. G. Nanobinders advance screen-printed flexible thermoelectrics. *Science* **2024**, *386*, 1265–1271.
[37] Zheng, Z. H.; Shi, X. L.; Ao, D. W.; Liu, W. D.; Li, M.; Kou, L. Z.; Chen, Y. X.; Li, F.; Wei, M.; Liang, G. X. et al. Harvesting waste heat with flexible Bi_2Te_3 thermoelectric thin film. *Nat. Sustain.* **2023**, *6*, 180–191.
[38] Zhang, T. Y.; Hao, S. W.; Yu, Y. R.; Hu, Z. Y.; Gu, L. Q.; Cong, H. L. Mechanically robust thermoelectric hydrogel with superior thermoelectricity for low-grade thermal energy harvesting and overheating warning. *ACS Appl. Mater. Interfaces* **2025**, *17*, 39503–39513.
[39] Cheng, H.; Du, Y. R.; Wang, B. J.; Mao, Z. P.; Xu, H.; Zhang, L. P.; Zhong, Y.; Jiang, W.; Wang, L. J.; Sui, X. F. Flexible cellulose-based thermoelectric sponge towards wearable pressure sensor and energy harvesting. *Chem. Eng. J.* **2018**, *338*, 1–7.
[40] Sun, Q.; Du, C. Y.; Huo, B. C.; Ding, Z. F.; Li, W. Q.; Chen, G. M. Radiation-modulated origami-based thermoelectric generator for continuous solar energy harvesting. *Adv. Funct. Mater.* **2026**, *36*, e18493.
[41] Zhang, L.; Shi, X. L.; Shang, H. J.; Gu, H. W.; Chen, W. Y.; Li, M.; Huang, D. X.; Dong, H.; Wang, X. L.; Ding, F. Z. et al. High-performance Ag_2Se-based thermoelectrics for wearable electronics. *Nat. Commun.* **2025**, *16*, 5002.
[42] Chen, W. Y.; Li, M.; Wang, X. D.; Otte, J.; Zhang, M.; Zhang, C. Y.; Cao, T. Y.; Hu, B. X.; Li, N. H.; Liu, W. D. et al. Flexible Ag_2Se-based thin-film thermoelectrics for sustainable energy harvesting and cooling. *Nat. Commun.* **2025**, *16*, 7579.
[43] Cao, T. Y.; Shi, X. L.; Hu, B. X.; Yang, Q. S.; Lyu, W. Y.; Sun, S.; Yin, L. C.; Liu, Q. Y.; Chen, W. Y.; Wang, X. D. et al. Advancing Ag_2Se thin-film thermoelectrics via selenization-driven anisotropy control. *Nat. Commun.* **2025**, *16*, 1555.
[44] Wu, Y.; Jiang, H.; Jiang, X. Y.; Liu, Y. L.; Zhang, X. W. Ag_2Se nanowire fusion-engineered nylon composite films: Boosting the stability and thermoelectric efficiency in flexible power generators. *ACS Appl. Mater. Interfaces* **2025**, *17*, 46218–46225.
[45] Zhou, Q.; Li, H. X.; Du, C. Y.; Ye, Z. Q.; Liang, L. R.; Chen, G. M. High-performance flexible thermoelectric generators with tunable in-plane and out-of-plane architectures. *Nano Energy* **2023**, *118*, 109007.
[46] He, X. Y.; Cai, J. X.; Liu, M. Y.; Ni, X. P.; Liu, W. D.; Guo, H. Y.; Yu, J. Y.; Wang, L. M.; Qin, X. H. Multifunctional, wearable, and wireless sensing system via thermoelectric fabrics. *Engineering* **2024**, *35*, 158–167.
[47] Luo, D.; Chen, H.; Chen, W. H.; Zhang, X. D.; Geng, L. M.; Jiang, W.; Yu, Y.; Cao, B. Y. Interdependent optimization strategies for material, module, and system designs in thermoelectric devices. *Device* **2025**, *3*, 100752.
[48] Yi, N. Z.; Zhang, C.; Wang, Z.; Zheng, Z. H.; Zhou, J. H.; Shang, R. Z.; Zhou, P. D.; Zheng, C.; You, M. H.; Chen, H. M. et al. Multi-functional $Ti_3C_2T_x$ -silver@Silk nanofiber composites with multi-dimensional heterogeneous structure for versatile wearable electronics. *Adv. Funct. Mater.* **2025**, *35*, 2412307.
[49] He, X. Y.; Shi, X. L.; Wu, X. Y.; Li, C. Z.; Liu, W. D.; Zhang, H. H.; Yu, X. L.; Wang, L. M.; Qin, X. H.; Chen, Z. G. Three-dimensional flexible thermoelectric fabrics for smart wearables. *Nat. Commun.* **2025**, *16*, 2523.
[50] Miao, L.; Zhu, S. J.; Liu, C. Y.; Gao, J.; Zhang, Z. W.; Peng, Y.; Chen, J. L.; Gao, Y. F.; Liang, J. S.; Mori, T. Comfortable wearable thermoelectric generator with high output power. *Nat. Commun.* **2024**, *15*, 8516.
[51] Hu, Y.; Wang, L.; Li, J.; Yang, Y. W.; Zhao, G. Y.; Liu, Y. M.; Huang, X. C.; Wu, P. C.; Zhang, B. B.; Jiao, Y. L. et al. Thin, soft, skin-integrated electronics for real-time and wireless detection of uric acid in sweat. *Int. J. Smart Nano Mater.* **2023**, *14*, 406–419.
[52] Zhao, Z. H.; Fu, H. R.; Tang, R. T.; Zhang, B. C.; Chen, Y. M.; Jiang, J. Q. Failure mechanisms in flexible electronics. *Int. J. Smart Nano Mater.* **2023**, *14*, 510–565.
[53] Feng, H. H.; Xiao, Y.; Yang, W. J.; Yang, H. T.; Zhou, R. H.; Lin, J. C.; Weng, M. C.; Chen, H. M.; Xu, Y. Maskless formation of patterned leather-based conductive electrode for human–computer interaction application. *Energy Mater.* **2025**, *5*, 500112.
[54] Zhou, P. D.; Yang, W. J.; Qiu, Y. H.; Xu, M. P.; Liao, L. T.; Gong, X. L.; Zheng, C.; You, M. H.; Zhang, C.; Chen, H. M. et al. Progress of MXenes-based responsive materials for soft sensors and actuators. *Responsive Mater.* **2026**, *4*, e70036.
[55] Guo, Z. H.; Zhang, Z. X.; An, K.; He, T. Y. Y.; Sun, Z. D.; Pu, X.; Lee, C. A wearable multidimensional motion sensor for AI-enhanced VR sports. *Research* **2023**, *6*, 0154.
[56] Niu, F.; Zhou, F. G.; Wang, Z. X.; Wei, L.; Hu, J.; Dong, L.; Ma, Y. F.; Wang, M.; Jia, S. T.; Chen, X. Y. et al. Synthesizing metal oxide semiconductors on doped Si/SiO_2 flexible fiber substrates for wearable gas sensing. *Research* **2023**, *6*, 0100.
[57] Fu, W. L.; Yu, B. Y.; Ji, D. X.; Zhou, Z.; Li, X. Y.; Wang, R.; Lu, W. B.; Sun, Y. M.; Dai, Y. Q. Intelligent fibers and textiles for wearable biosensors. *Responsive Mater.* **2024**, *2*, e20240018.